occupation after a time evolution of 2 s, when collective spin oscillations have been damped out already and the system is in a quasi-equilibrium configuration. We identify three different regions: (i) the Zeeman-protected regime, where spin-changing collisions are off-resonant and the spin configuration remains constant; (ii) the spin-oscillation regime, where spin-changing collisions are resonant and spin instabilities occur; and (iii) a stable high-density regime, where the spin configuration does not change, despite the fact that coherent spin-changing oscillations would be resonant, thus possible. To illustrate the behavior in regime (iii) more clearly, we show time evolutions at different magnetic fields for two slightly different densities (Fig. 4, B and C), revealing an abrupt spin stabilization at small magnetic fields for the larger density. We attribute this stabilization to an increased rate of incoherent collisions at large densities. In terms of the single-particle density matrix formalism, these incoherent collisions project the initial state onto the diagonal elements, which is similar to the measurement projection associated with the quantum-Zeno effect. In further analogy, any coherent evolution is suppressed. In the experiments presented here, this mechanism is highly sensitive to slight changes of the experimental parameters and leads to a completely different macroscopic behavior of the Fermi sea.

We have investigated the intriguing interplay between several microscopic spin-changing processes in ultracold high-spin Fermi gases. The high experimental control as well as the obtained understanding of our model system, opens the path to studying exotic phenomena, such as the creation of topological structures and textures in superfluid Fermi gases with high spin.

References and Notes

1. C. A. Regal, M. Greiner, D. S. Jin, *Phys. Rev. Lett.* **92**, 040403 (2004).
2. M. W. Zwierlein, J. R. Abo-Shaeer, A. Schirotzek, C. H. Schunck, W. Ketterle, *Nature* **435**, 1047–1051 (2005).
3. U. Schneider *et al.*, *Science* **322**, 1520–1525 (2008).
4. R. Jördens, N. Strohmaier, K. Günter, H. Moritz, T. Esslinger, *Nature* **455**, 204–207 (2008).
5. N. Navon, S. Nascimbène, F. Chevy, C. Salomon, *Science* **328**, 729–732 (2010); 10.1126/science.1187582.
6. A. Sommer, M. Ku, G. Roati, M. W. Zwierlein, *Nature* **472**, 201–204 (2011).
7. M. Koschorreck, D. Pertot, E. Vogt, M. Köhl, *Nat. Phys.* **9**, 405–409 (2013).
8. L. A. Sidorenkov *et al.*, *Nature* **498**, 78–81 (2013).
9. X. Du, L. Luo, B. Clancy, J. E. Thomas, *Phys. Rev. Lett.* **101**, 150401 (2008).
10. M. J. Martin *et al.*, *Science* **341**, 632–636 (2013).
11. G.-B. Jo *et al.*, *Science* **325**, 1521–1524 (2009).
12. D. Greif, T. Uehlinger, G. Jotzu, L. Tarruell, T. Esslinger, *Science* **340**, 1307–1310 (2013); 10.1126/science.1236362.
13. T.-L. Ho, S. Yip, *Phys. Rev. Lett.* **82**, 247–250 (1999).
14. P. Lecheminant, E. Boulat, P. Azaria, *Phys. Rev. Lett.* **95**, 240402 (2005).
15. C. Wu, *Phys. Rev. Lett.* **95**, 266404 (2005).
16. A. Rapp, G. Zaránd, C. Honerkamp, W. Hofstetter, *Phys. Rev. Lett.* **98**, 160405 (2007).
17. M. A. Cazalilla, A. F. Ho, M. Ueda, *New J. Phys.* **11**, 103033 (2009).
18. A. V. Gorshkov *et al.*, *Nat. Phys.* **6**, 289–295 (2010).
19. K. Rodríguez, A. Argüelles, M. Colomé-Tatché, T. Vekua, L. Santos, *Phys. Rev. Lett.* **105**, 050402 (2010).
20. Y. Dong, H. Pu, *Phys. Rev. A* **87**, 043610 (2013).
21. D. M. Stamper-Kurn, M. Ueda, *Rev. Mod. Phys.* **85**, 1191–1244 (2013).
22. Y. Kawaguchi, M. Ueda, *Phys. Rep.* **520**, 253–381 (2012).
23. J. S. Krauser *et al.*, *Nat. Phys.* **8**, 813–818 (2012).
24. S. Taie, R. Yamazaki, S. Sugawa, Y. Takahashi, *Nat. Phys.* **8**, 825–830 (2012).
25. T. Lompe *et al.*, *Science* **330**, 940–944 (2010).
26. J. Heinze *et al.*, *Phys. Rev. Lett.* **110**, 250402 (2013).
27. Supplementary materials are available on *Science* Online.
28. C. S. Gerving *et al.*, *Nat. Commun.* **3**, 1169 (2012).
29. U. Ebling, A. Eckardt, M. Lewenstein, *Phys. Rev. A* **84**, 063607 (2011).
30. C. Lhuillier, F. Laloë, *Phys. Rev. Lett.* **54**, 1207 (1985).
31. T. Nikuni, J. E. Williams, C. W. Clark, *Phys. Rev. A* **66**, 043411 (2002).
32. H. K. Pechkis *et al.*, *Phys. Rev. Lett.* **111**, 025301 (2013).
33. C. Deutsch *et al.*, *Phys. Rev. Lett.* **105**, 020401 (2010).

Performing Mathematical Operations with Metamaterials

Alexandre Silva,[1]* Francesco Monticone,[2]* Giuseppe Castaldi,[3] Vincenzo Galdi,[3] Andrea Alù,[2] Nader Engheta[1]†

We introduce the concept of metamaterial analog computing, based on suitably designed metamaterial blocks that can perform mathematical operations (such as spatial differentiation, integration, or convolution) on the profile of an impinging wave as it propagates through these blocks. Two approaches are presented to achieve such functionality: (i) subwavelength structured metascreens combined with graded-index waveguides and (ii) multilayered slabs designed to achieve a desired spatial Green's function. Both techniques offer the possibility of miniaturized, potentially integrable, wave-based computing systems that are thinner than conventional lens-based optical signal and data processors by several orders of magnitude.

Metamaterials—artificially engineered structures designed to exhibit unconventional wave properties—have recently opened exciting venues for unprecedented control and manipulation of electromagnetic fields, as well as other forms of waves, such as acoustic, elastic, mechanical, and matter waves (*1–5*). The spatial and/or temporal engineering of their bulk parameters, such as the permittivity and permeability of an artificial material, enables shaping of local and global field distributions to achieve a desired functionality. Transformation optics (*6, 7*), for instance, has shown that by locally tailoring the electric and magnetic response of a material, one may be able to achieve functionalities of interest, such as cloaking (*6–8*), field concentration or rerouting (*9–14*), and optical illusions (*15*).

Here, we introduce the concept of "computational metamaterials" that can be used to perform mathematical operations—such as spatial differentiation, integration, or convolution—as electromagnetic waves propagate through them. Traditional analog computers, or "calculating machines" in the form of mechanical, electronic, and hybrid analog computers, have been designed in the past to perform such mathematical computations (*16–18*), but these solutions have suffered from substantial limitations, including relatively large size and slow response. Mechanical deformation of arrays of bars and pivots to achieve a certain functional response (*19*) and construction of linkages to synthesize a portion of an algebraic curve (*20*) have also been explored. Our idea for metamaterial-based computing is conceptually sketched in Fig. 1, in which metamaterial blocks produce a wave profile at their output proportional to the desired operation performed on an arbitrary input wave profile by suitably manipulating the impinging wave as it propagates through them. Although a selected set of these functionalities may be achieved with well-known optical signal processing or Fourier optics using conventional lenses (*21–23*), our approaches provide the possibility of highly compact, potentially integrable architectures with-

[1]Department of Electrical and Systems Engineering, University of Pennsylvania, Philadelphia, PA 19104, USA. [2]Department of Electrical and Computer Engineering, University of Texas, Austin, TX 78712, USA. [3]Waves Group, Department of Engineering, University of Sannio, Benevento I-82100, Italy.

*These authors contributed equally to this work.
†Corresponding author. E-mail: engheta@ee.upenn.edu

in much smaller volumes and, in some cases, over subwavelength thicknesses, ensuring controlled manipulation and processing of the incoming signal.

We introduce two approaches to computational metamaterials: (i) a metasurface (MS) approach, in which thin planar metamaterial blocks perform mathematical operations in the spatial Fourier domain and (ii) a Green's function (GF) approach, in which multilayered metamaterial slabs realize a desired GF (i.e., spatial impulse response) at the output, allowing the synthesis of mathematical operations of interest. For simplicity, we focus on

metamaterials that realize linear, shift-invariant operations on transverse spatial variables, assuming $\exp(-i\omega t)$ monochromatic signals. Without loss of generality, we assume two-dimensional scenarios in which wave signals and the metamaterial parameters depend only on the longitudinal direction of propagation x and one transverse coordinate y.

We base our first (MS) approach on the fact that the linear convolution $g(y) = \int f(u)G(y - u)du$ between an arbitrary field distribution $f(y)$ and the GF $G(y)$ associated with the operator of choice may be expressed in the spatial Fourier space as

$\tilde{g}(k_y) = \tilde{G}(k_y)\tilde{f}(k_y)$, where the tilde indicates Fourier transform. In this approach, our metamaterial system consists of three cascaded subblocks: (i) a Fourier transform subblock, (ii) a suitably tailored MS spatial filter that applies the $\tilde{G}(k_y)$ operation in the Fourier domain, and (iii) an inverse Fourier transform subblock (Fig. 2A). For the first subblock, we consider a two-dimensional graded-index (GRIN) dielectric slab with permeability $\mu = \mu_0$ and a parabolic variation of permittivity

$$\varepsilon(y) = \varepsilon_c \left[1 - \left(\frac{\pi}{2L_g} \right)^2 y^2 \right] \quad (1)$$

where ε_c is the permittivity at the central plane of the GRIN and L_g is the characteristic length (24). In Fig. 2A, GRIN(+) indicates a conventional GRIN, with (+) referring to permittivity and permeability being positive. In the paraxial approximation, the GRIN(+) slab operates as a Fourier transformer at the "focal" length L_g along the direction of propagation (24). For the inverse Fourier transform [subblock GRIN(−)], we use an ideal GRIN structure with negative parameters: permeability $\mu = -\mu_0$ and permittivity $\varepsilon = -\varepsilon(y)$. Following the concept of complementary materials (25), the GRIN(−) has the inverse functionality of the GRIN(+); that is, it acts as an inverse Fourier transformer.

The metastructure screen is designed using two different approaches (insets in Fig. 2A): (i) a "conceptual" thin MS with volumetric parameters $\varepsilon_{ms}(y)/\varepsilon_0 = \mu_{ms}(y)/\mu_0$ (left inset) and (ii) a realistic three-layered thin metamaterial

Fig. 1. Wave-based metamaterial computing. A conceptual sketch of a suitably designed metamaterial block that may perform a desired mathematical operation on arbitrary wave signals as they propagate through it.
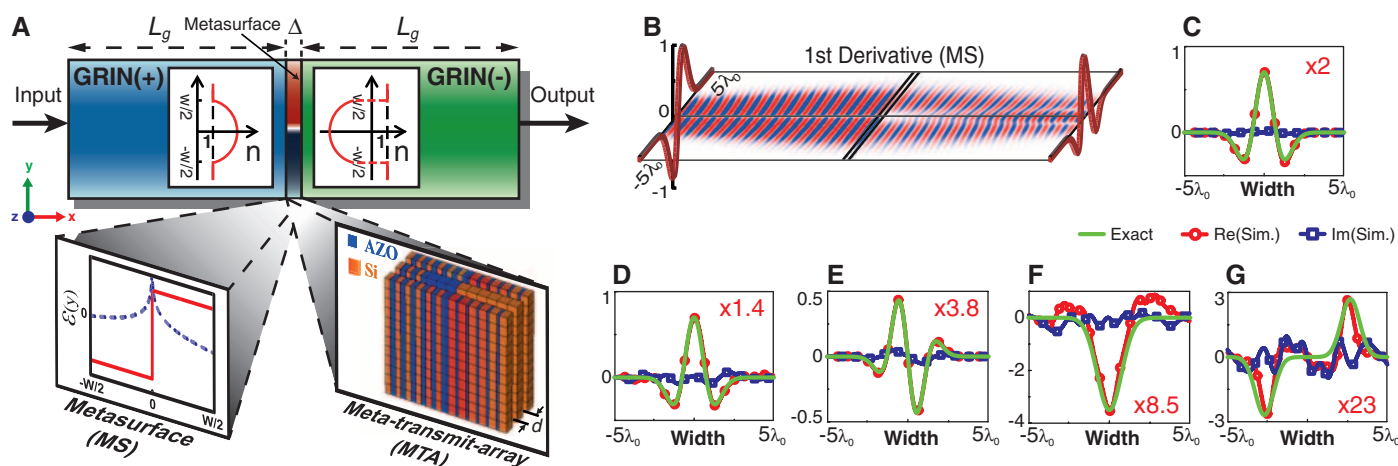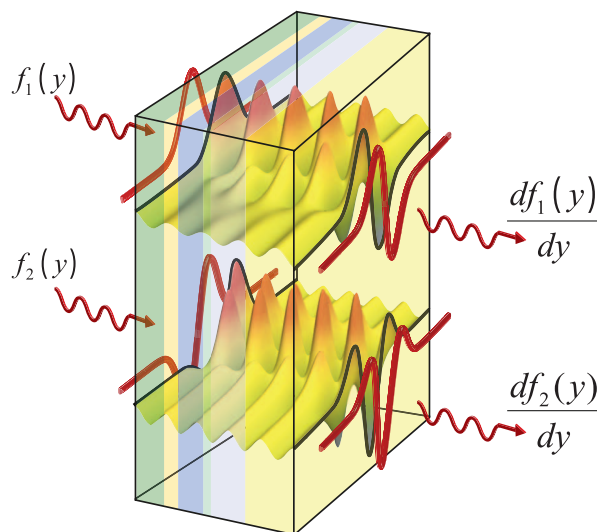
Fig. 2. Metamaterial computing using metasurfaces. (**A**) A thin, properly designed metastructure screen with thickness $\Delta = \lambda_0/3$ and width $W \approx 10\lambda_0$, sandwiched between two GRIN structures with positive and negative parameters, can perform mathematical operations in the Fourier domain. The GRIN(+) and GRIN(−), each with length $L_g \approx 12\lambda_0$, act as Fourier and inverse Fourier transformers. Two designs are proposed for the middle metastructure: a thin MS formed by a single layer with prescribed permittivity and permeability [left inset, with real (red) and imaginary (blue) parts of material parameters] and a realistic metatransmit-array (MTA) formed by three sublayers made of two alternating materials (here, Si and AZO) with properly prescribed inhomogeneous distribution of their volume filling fractions, and with required loss to impart the desired attenuation (right inset) (28). This system forms a computational metamaterial unit that can perform mathematical operations of choice on the input function as the wave propagates through it. (**B**) Perspective view of the input function is shown at left, along with a snapshot of our simulation results for the z-component of the electric field throughout the metamaterial system functioning as first differentiator using MS. The output profile is shown at right. (**C** to **G**) Simulation results [real (red) and imaginary (blue) parts] at the output of our computational metastructures for (C) first differentiation, (E) second differentiation, (F) integration, and (G) convolution operators, all using MS; and (D) first differentiation using MTA [with both GRIN sections being GRIN(+)]. All simulated outputs are compared with the expected analytical results (green). For easy comparison, output results in each panel are multiplied by a constant factor (shown in each plot) and proper phase adjustments (28) are applied: (C) 8°, (D) −15°, (E) 0°, (F) −8°, (G) 18°.

based on an appropriate alternation of two materials—in this case, aluminum-doped zinc oxide (AZO) (26) and silicon (Si)—with different levels of loss (right inset). Our "meta-transmit-array" (MTA) design is inspired by (27) and is extended to the present case (28) so as to control both phase and magnitude of the transmitted wave according to the desired local transfer function $\tilde{G}(k_y)$ while minimizing reflections. We apply these concepts to realize some fundamental mathematical operators.

First-order derivative: $g(y) \propto df(y)/dy$. In this case, $\tilde{G}(k_y) \propto (ik_y)$ and we first consider a transversely inhomogeneous MS with thickness $\Delta < \lambda_0$ (where λ_0 is the free-space wavelength), in which the transverse coordinate y plays the role of k_y. The relative permittivity and permeability of such a MS (laterally limited to $|y| \leq W/2$), required to achieve the normalized transfer function proportional to $iy/(W/2)$, are (28)

$$\frac{\varepsilon_{ms}(y)}{\varepsilon_0} = \frac{\mu_{ms}(y)}{\mu_0} = i\left(\frac{\lambda_0}{2\pi\Delta}\right)\ln\left(\frac{-iW}{2y}\right) \quad (2)$$

Once this subblock is sandwiched between a GRIN(+) and a GRIN(−), each one with length L_g, we obtain a first-differentiator metamaterial system. Figure 2B shows our numerical simulation for the input function $f(y) = ay \exp(-y^2/b)$ with $a = 0.7 \, \mu m^{-1} = 2.1\lambda_0^{-1}$ and $b = 10 \, \mu m^2 = \lambda_0^2/0.9$, used to test all the operators in Fig. 2. In this set of simulations, we assume $\lambda_0 = 3 \, \mu m$, $W = 29.75 \, \mu m \approx 10\lambda_0$, $L_g = 35 \, \mu m \approx 12\lambda_0$, $\varepsilon_c = 2.01\varepsilon_0$, and $\Delta = 1 \, \mu m = \lambda_0/3$. Although this design principle can be applied to any wavelength, here we have chosen to operate at infrared frequencies, which are of interest for various applications; this allows us to use realistic CMOS (complementary metal-oxide semiconductor)–compatible materials. The input function, depicted in perspective at the left of Fig. 2B, is the z-component of the electric field distribution at the entrance of this metamaterial system. We also show the distribution (snapshot in time) of this field component as the wave propagates through the entire system. At the output plane ($2L_g + \Delta$), we obtain the electric field distribution $g(y)$ shown also in Fig. 2C, which is indeed closely proportional to the first spatial derivative of the input function (green line).

To get closer to a practical realization, we also consider the more realistic MTA design and replace the ideal GRIN(−) subblock with a GRIN(+), exploiting the relation $\mathcal{F}\{\mathcal{F}[g(y)]\} \propto g(-y)$, with $\mathcal{F}(\cdot)$ denoting Fourier transform, thereby expecting the output function to be proportional to a "mirror image" of the desired result. Simulation results for this scenario (Fig. 2D) are clearly proportional to the analytical result.

Second-order derivative: $g(y) \propto d^2f(y)/dy^2$. A metamaterial that performs second spatial differentiation could be designed as a cascade of two first-differentiator blocks. However, to demonstrate the generality of our concept, we design a MS that directly performs the second differen-

tiation. Thanks to our "modular" scheme, we simply replace the MS subblock by another one with the desired transfer function $[iy/(W/2)]^2$, which requires volumetric permittivity and permeability functions

$$\frac{\varepsilon_{ms}(y)}{\varepsilon_0} = \frac{\mu_{ms}(y)}{\mu_0} = i2\left(\frac{\lambda_0}{2\pi\Delta}\right)\ln\left(\frac{-iW}{2y}\right) \quad (3)$$

for $|y| \leq W/2$. Figure 2E presents our numerical simulation for this case, confirming excellent functionality.

Integration: $g(y) \propto \int f(y)dy$. For this operation, the MS subblock needs to implement the transfer function $(iy/d)^{-1}$, where $d = 1 \, \mu m$ is an arbitrary normalizing length. To avoid gain requirements for transmission coefficients with magnitude larger than unity for $|y| < d$, we truncate the

required transfer function at $|y| = d$ and assume its magnitude to be unity within this range. Therefore, the MS has volumetric constitutive parameters

$$\frac{\varepsilon_{ms}(y)}{\varepsilon_0} = \frac{\mu_{ms}(y)}{\mu_0} = i\left(\frac{\lambda_0}{2\pi\Delta}\right)\ln\left(\frac{iy}{d}\right) \quad (4)$$

for $|y| > d$, and

$$\frac{\varepsilon_{ms}(y)}{\varepsilon_0} = \frac{\mu_{ms}(y)}{\mu_0} = -\left(\frac{\lambda_0}{4\Delta}\right)sgn\left(\frac{y}{d}\right) \quad (5)$$

for $|y| < d$. Figure 2F presents the simulation results for the integral operation performed by this structure compared with the expected result, again demonstrating good functionality.

Convolution: $g(y) = \int f(u)G(y-u)du$. We also design a MS that performs convolution with a rectangular kernel of width $W_k = 16 \, \mu m = 5.33\lambda_0$. As before, our MS realizes a transfer function
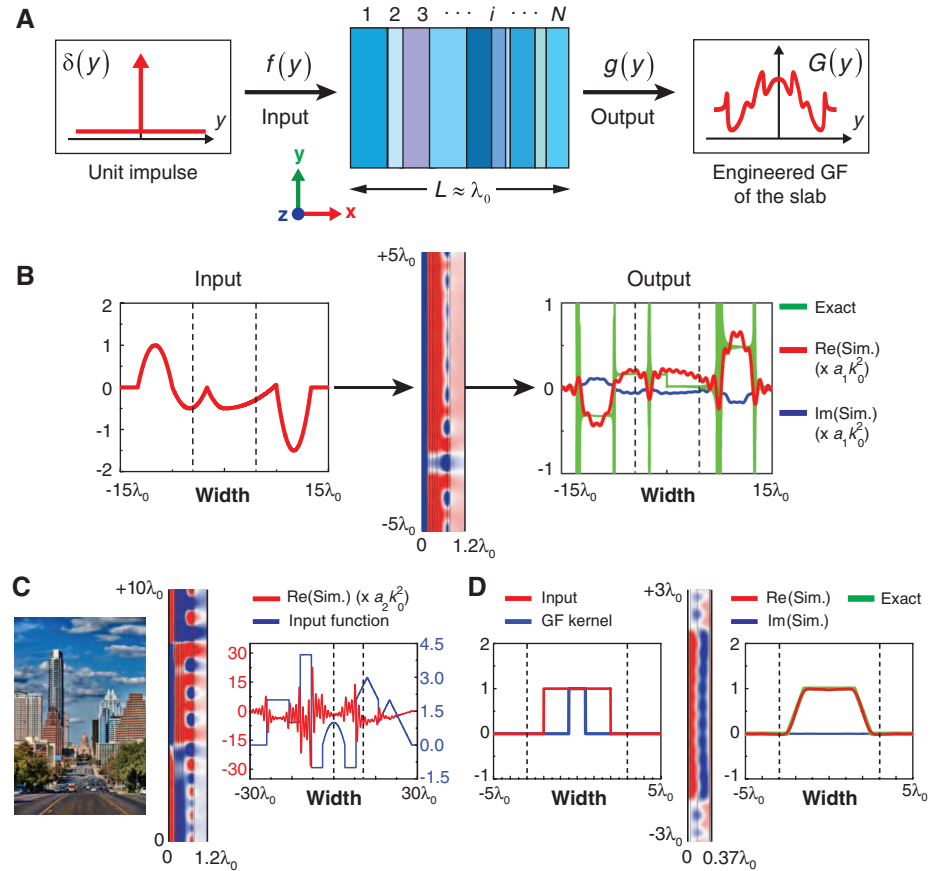
Fig. 3. Metamaterial computing using Green's function slabs. (**A**) A multilayered slab is designed to exhibit the desired GF kernel associated with a mathematical operation of choice. (**B** and **C**) Ten-layered nonmagnetic GF slab designed to perform second spatial differentiation (28). Simulated wave propagation (z-component of the magnetic field) throughout the slab for two different input functions: (B) a set of quadratic polynomial functions, and (C) Austin city skyline. The right panel in (B) shows the comparison between simulated output (red, real part; blue, imaginary part) and the analytical (green) results, whereas in (C) the real part of the simulated output (red) is directly compared to the input function (blue) to highlight the correspondence between the input edges and the sharp peaks at the output. In each panel, the simulation result is multiplied by a constant factor (noted in parentheses) for easy comparison. (**D**) Five-layered GF slab (28) designed to perform the convolution with a rectangular kernel of width λ_0, shown in blue in the left panel, for a rectangular input function of width $4\lambda_0$ (red line). In (B) to (D), the snapshots of field distributions are shown in a limited lateral region for clarity, indicated by the dashed lines. [Austin city skyline photo courtesy of Tod Grubbs of Bee Creek Photography, reproduced with permission]

corresponding to the Fourier transform of the kernel

$$\tilde{G}(y) = \mathrm{sinc}\left(\frac{W_k y}{2s^2}\right) \qquad (6)$$

where

$$s = \sqrt{\frac{\lambda_0 L_g}{\pi^2 \sqrt{\varepsilon_c / \varepsilon_0}}} \qquad (7)$$

is a GRIN scale factor defined in (24). For such a transfer function, the required constitutive parameters are

$$\frac{\varepsilon_{ms}(y)}{\varepsilon_0} = \frac{\mu_{ms}(y)}{\mu_0}$$
$$= i\left(\frac{\lambda_0}{2\pi\Delta}\right)\ln\left[\frac{1}{\mathrm{sinc}(W_k y / 2s^2)}\right] \qquad (8)$$

The results of our simulation are shown in Fig. 2G, demonstrating good agreement with the analytical results.

In our second (GF) approach, we design a multilayered metamaterial slab, transversely homogeneous but longitudinally inhomogeneous, that realizes an output field distribution $g(y)$ to an input function $f(y)$, consistent with the GF $G(y)$ associated with a desired operator of choice (Fig. 3A). In this approach, we avoid the need of going into the Fourier domain, hence avoiding the GRIN subblocks that perform Fourier and inverse Fourier transforms. Because this GF slab is transversely symmetric, it can in principle realize an arbitrary GF with even symmetry, such as the second spatial derivative $g(y) \propto d^2 f(y)/dy^2$, which can be written in terms of an even kernel as $g(y) \propto \int f(u)\delta''(y-u)du$ [where the required GF is proportional to the second spatial derivative of the Dirac delta function $\delta''(y)$]. Our goal is then to tailor the transmission coefficient for impinging plane waves as a function of the transverse wavenumber k_y to be $\tilde{G}(k_y) \propto -k_y^2$. In (29), we addressed this problem within the framework of nonlocal transformation optics, assuming infinite media. Here, we consider a finite longitudinal thickness divided into N parallel layers with subwavelength thicknesses d_i, $i = 1, 2, \ldots, N$ (Fig. 3A). We developed a fast synthesis approach to obtain the permittivity, permeability, and thickness of each layer required to tailor the overall plane-wave transmission coefficient to match $\tilde{G}(k_y)$ for all impinging angles (28). It is also possible to obtain the same result using nonmagnetic layered metamaterials by suitably increasing the number of layers, arguably simplifying the design and bringing it closer to practical realization. The 10-layered design (28) in Fig. 3B is a GF slab with nonmagnetic ($\mu = \mu_0$) constitutive parameters and an overall thickness comparable to λ_0.

Our numerical results confirm that the designed metamaterial provides a GF kernel that resembles, given the unavoidable limited resolution, the desired $\delta''(y)$ at the output plane when the input is an approximate delta function. In Fig. 3, B and C, we apply a set of quadratic poly-

nomial functions and the Austin city skyline borders, respectively, as inputs for our second-spatial-derivative GF slab, showing the evolution of the z-component of the magnetic field distribution along the slab, and demonstrating that the designed structure indeed approximately performs the second-derivative operation as the wave propagates through it. Edge-detection spatial analog filters [e.g., Laplace filters (30)] and image-processing devices may largely benefit from this system. We also design a five-layered GF slab (with overall thickness of $0.37\lambda_0$) that performs the convolution operation of an input function with a one-wavelength rectangular spatial kernel (28). Figure 3D shows the simulation results using another rectangular function as input.

Our proposed computational metastructures are smaller than conventional lens-based optical signal-processing systems by several orders of magnitude. Moreover, with no analog-to-digital conversion or other systematic delays, here mathematical operations get processed as the electromagnetic signals propagate through the highly miniaturized and compact computational metamaterials. Such designs may potentially lead to direct, ultrafast, wave-based analog computation, equation solving, and signal processing at the hardware level.

References and Notes

1. N. Engheta, R. W. Ziolkowski, Eds., *Metamaterials—Physics and Engineering Explorations* (IEEE-Wiley, New York, 2006).
2. G. V. Eleftheriades, K. G. Balmain, *Negative-Refraction Metamaterials* (IEEE, New York, 2005).
3. D. R. Smith, J. B. Pendry, M. C. K. Wiltshire, *Science* **305**, 788–792 (2004).
4. C. Caloz, T. Itoh, *Electromagnetic Metamaterials—Transmission Line Theory and Microwave Applications* (IEEE-Wiley, New York, 2006).
5. W. Cai, V. Shalaev, *Optical Metamaterials: Fundamentals and Applications* (Springer, New York, 2010).
6. J. B. Pendry, D. Schurig, D. R. Smith, *Science* **312**, 1780–1782 (2006).
7. U. Leonhardt, *Science* **312**, 1777–1780 (2006).
8. A. Alù, N. Engheta, *Phys. Rev. E* **72**, 016623 (2005).
9. A. Vakil, N. Engheta, *Science* **332**, 1291–1294 (2011).
10. E. F. Kuester, M. A. Mohamed, M. Piket-May, C. L. Holloway, *IEEE Trans. Antenn. Propag.* **51**, 2641–2651 (2003).
11. N. Yu *et al.*, *Science* **334**, 333–337 (2011).
12. X. Ni, N. K. Emani, A. V. Kildishev, A. Boltasseva, V. M. Shalaev, *Science* **335**, 427 (2012).
13. Y. Zhao, M. A. Belkin, A. Alù, *Nat. Commun.* **3**, 870 (2012).
14. A. Pandey, N. M. Litchinitser, *Opt. Lett.* **37**, 5238–5240 (2012).
15. Y. Lai *et al.*, *Phys. Rev. Lett.* **102**, 253902 (2009).
16. D. de Solla Price, *IEEE Micro.* **4**, 22–52 (1984).
17. A. B. Clymer, *IEEE Ann. Hist. Comput.* **15**, 19 (1993).
18. Computer History Museum, www.computerhistory.org/revolution/analog-computers/3.
19. G. W. Milton, *J. Mech. Phys. Solids* **61**, 1543–1560 (2013).
20. A. B. Kempe, *Proc. London Math. Soc.* **7**, 213 (1876).
21. A. Weiner, *Rev. Sci. Instrum.* **71**, 1929 (2000).
22. D. Casasent, *Proc. IEEE* **65**, 143–157 (1977).
23. J. Goodman, *Introduction to Fourier Optics* (Roberts & Co., Englewood, CO, ed. 3, 2005).
24. H. M. Ozaktas, D. Mendlovic, *J. Opt. Soc. Am. A* **10**, 2522 (1993).
25. J. B. Pendry, S. A. Ramakrishna, *J. Phys. Condens. Matter* **15**, 6345–6364 (2003).
26. G. V. Naik, J. Kim, A. Boltasseva, *Opt. Mater. Express* **1**, 1090 (2011).
27. F. Monticone, N. M. Estakhri, A. Alù, *Phys. Rev. Lett.* **110**, 203903 (2013).
28. See supplementary materials on *Science* Online.
29. G. Castaldi, V. Galdi, A. Alù, N. Engheta, *Phys. Rev. Lett.* **108**, 063902 (2012).
30. R. C. Gonzalez, R. E. Woods, *Digital Image Processing* (Prentice Hall, New York, 2008).

Heteroepitaxial Growth of Two-Dimensional Hexagonal Boron Nitride Templated by Graphene Edges

Lei Liu,[1]* Jewook Park,[2]* David A. Siegel,[3] Kevin F. McCarty,[3] Kendal W. Clark,[2] Wan Deng,[1] Leonardo Basile,[2,4] Juan Carlos Idrobo,[2] An-Ping Li,[2]† Gong Gu[1]†

By adapting the concept of epitaxy to two-dimensional space, we show the growth of a single-atomic-layer, in-plane heterostructure of a prototypical material system—graphene and hexagonal boron nitride (h-BN). Monolayer crystalline h-BN grew from fresh edges of monolayer graphene with atomic lattice coherence, forming an abrupt one-dimensional interface, or boundary. More important, the h-BN lattice orientation is solely determined by the graphene, forgoing configurations favored by the supporting copper substrate.

In conventional heteroepitaxial growth, an extended single-crystal film, or epilayer, forms on a two-dimensional (2D) surface of a single crystal of a different material, as exemplified by

the growth of GaAs on Si (1). In general, if the lattice constants of the different materials are similar, the atomic lattice of the surface can act as a template for the initial growth of the